BL33XU
TOYOTA

1. Introduction

BL33XU, the Toyota beamline, was built in FY2009 and is operated by Toyota Central R&D Labs., Inc. [1]. The original purpose of this beamline was to perform quick-scanning X-ray absorption spectroscopy (QXAFS) for *operando* analysis and three-dimensional X-ray diffraction (3DXRD). These techniques were not available at SPring-8 before 2009 and were needed for industrial applications. In addition to these, the following techniques have been adopted: X-ray diffraction (XRD), X-ray computed tomography (CT)/ laminography, and small-angle X-ray scattering (SAXS), as shown in Fig. 1. In this report, we describe the current status of this beamline and recent technical progress.

2. BL33XU Beamline

2-1. Beamline layout

The medium-length beamline of BL33XU has the optics hutch in the storage ring building of SPring-8. The experimental facility building is located outside the storage ring building. The building has three experimental hutches, a chemical laboratory and an office room.

The layout of optical components of BL33XU, where two different types of monochromators are installed, is shown in Fig. 2. Optics 1 is mainly used for QXAFS. It is composed of horizontal deflection mirrors (M1 and M2) in the optics hutch, compact monochromators (C-Mono) with channel-cut crystals, and vertical total reflection mirrors (M3 and M4) in EH1. Optics 2 is used for 3DXRD and other techniques. It consists of a SPring-8 standard double-crystal monochromator, vertical total reflection mirrors (M4 and M5), and Kirkpatrick–Baez focusing mirrors (KBMs) that yield a 1-μm-square microbeam at 50 keV in EH3.

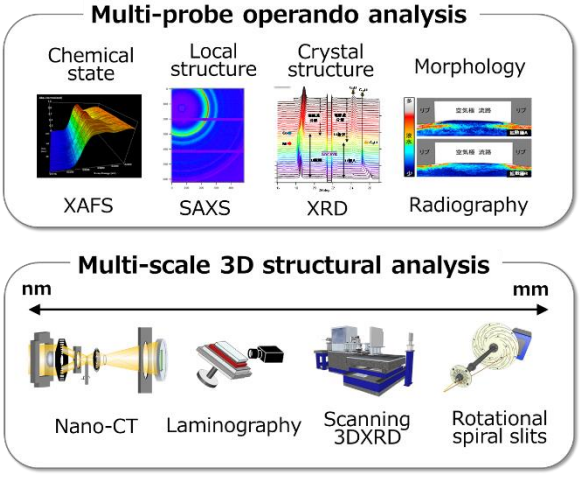

Fig. 1. Measurement techniques at BL33XU.

2-2. Analysis techniques

(1) QXAFS

A tapered undulator combined with the servo-motor-driven channel-cut monochromator realizes rapid data acquisition of XAFS with a temporal resolution of 10 ms [2]. The energy range from 4.0 to 45 keV is attained by the two monochromators with Si(111) and Si(220) crystals. This QXAFS system has enabled the development of various *in*

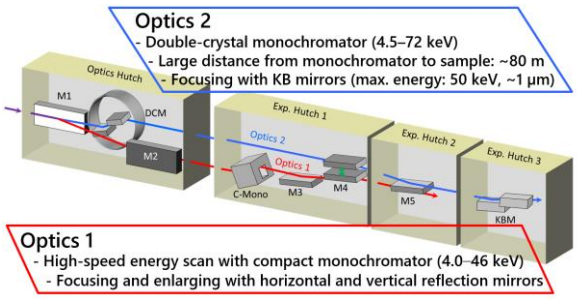

Fig. 2. Optical components of BL33XU.

situ measurement techniques such as simultaneous XAFS and XRD measurements of positive and negative electrodes of lithium-ion batteries during charging and discharging [3].

(2) SAXS

The camera distance from tens of centimeters to 4.5 meters can be selected for SAXS at BL33XU. A two-dimensional detector, PILATUS 300K (Dectris), is available for the developed *in situ* measurement system. An example of use is an *in situ* measurement to analyze the structural evolution of resins during the injection molding process [4].

(3) XRD

For the analysis of the reliability of mechanical and electronic components, it is important to measure the internal stresses and strains nondestructively. A measurement based on XRD was realized by using a multi-axial goniometer equipped with a proprietary developed rotating and revolving spiral slits system. The rotating shield disks with the slits enable the detection of diffraction only from a small gage volume of interest inside a component with a two-dimensional detector, PILATUS. This system realizes the depth-resolved distribution measurement of strain in an actual mechanical component [5].

(4) Scanning 3DXRD

In order to measure the three-dimensional distribution of stresses inside the grains of a bulk sample, i.e., type III stresses, the 3DXRD microscopy methodology was developed [6]. This nondestructive technique was validated in 2013 and the three-dimensional distribution of stresses inside the grains of bulk polycrystalline steel under tensile deformation was measured in 2019 [7]. The results revealed that the microscopic intragranular stresses greatly deviate from the macroscopic average stresses measured by conventional methods. Combined with other nondestructive measurement techniques such as XRD and laminography, 3DXRD is expected to facilitate the development of multi-scale material modeling that expresses deformation, fracture, and life of components.

(5) X-ray CT and laminography

In order to meet the growing need for the high-resolution nondestructive observation of internal behavior in mechanical and electronic components, X-ray CT and laminography techniques were introduced. The resolutions of the two imaging techniques are less than 1 μm even under *in situ* measurement where sample materials and components are exposed to actual working conditions. In addition, a nano-CT system with a Fresnel zone plate (FZP) has achieved a resolution of ~100 nm [8].

3. Recent technological progress: 3D water management in polymer electrolyte fuel cells toward fuel cell electric vehicles [9]

The global shift from internal combustion engine vehicles to battery electric vehicles (BEVs) and fuel cell electric vehicles (FCEVs) is accelerating. FCEVs offer many advantages over BEVs, including long range, short refueling time, and high efficiency even at sub-zero temperatures. Since the release of the first-generation MIRAI in 2014, Toyota Group companies have leveraged the development and promotion of FCEVs towards a hydrogen-based society. As a result, the second-generation MIRAI, which was launched in 2020, has achieved a maximum power density of 5.4 kW L^{-1} (excluding end plates), a 50% improvement over the first-generation MIRAI.

The first step in the improvement of the fuel

cell performance of polymer electrolyte fuel cells (PEFCs) for FCEVs is to increase the mass activity of the catalysts for the oxygen reduction reaction. State-of-the-art catalysts with mass activities 10 times higher than those of commercially available platinum catalysts have been demonstrated at the laboratory scale using rotating desk electrodes (RDEs). However, owing to various factors such as catalyst poisoning and harsh conditions when using membrane electrode assemblies (MEAs), these catalysts exhibit lower mass activities than do those using RDEs. In addition, an ionomer–platinum interface induces local oxygen transport resistance in the MEA, leading to performance degradation. Therefore, the use of hand-sized PEFCs, typically less than 10 cm^2, to evaluate fuel cell performance is the next step. However, increasing the fuel cell performance of hand-sized PEFCs at high current densities will not improve the performance of hand-sized PEFCs in FCEVs. As the size of the PEFC increases, the large amount of water produced inhibits the oxygen supply to the catalyst in the MEA, leading to a voltage drop during high-current-density operation. The chemical engineering gap for automotive applications needs to be addressed by considering "drainability", that is, the ability to drain the produced water from PEFCs.

We present techniques for visualizing water using a combination of operando neutron and synchrotron X-ray radiography established at J-PARC and SPring-8. We observe the water behavior in both practical-size and hand-sized PEFCs under similar operating conditions. Our aim is to investigate the origins of the drainability of a second-generation MIRAI fuel cell.

For operando neutron imaging, we performed the operation at a constant current density of 1.47 A cm^{-2} and a temperature of 60 °C. Even after the steady state was reached, a nonuniform distribution of water was observed inside the PEFC of practical size, especially at the top (position 1) and bottom (position 4) of the PEFC center [Fig. 3(a)], corresponding to the temperature distribution. The amount of produced water increased up to a distance of x = 180 mm downstream of the cathode. In contrast, near the cathode outlet (x = 210 mm), the amount of produced water decreased, suggesting that some of the produced water was transported towards the anode outlet (i.e., cathode inlet) because of water backdiffusion.

For operando synchrotron X-ray radiography, the hand-sized PEFC was operated at a constant current density of 1.47 A cm^{-2} and a temperature of 60 °C, and had the same current density as the practical PEFC. The water content of the cathode was evaluated at different levels of relative humidity in order to simulate the environment of the practical PEFC. Figure 3(b) shows the cross-sectional distribution of water in the interior of the hand-sized PEFC at 120% RH (i.e., condensing). The water-layer thickness relative to the X-ray path length was converted to the water content in the through-plane direction for comparison with the neutron radiography data. The converted water content, in agreement with the results of the neutron radiography experiment, was typically <3 mg cm^{-2}. Neutron radiography did not confirm water blocking in the gas channels of the practical size PEFC under the present operating conditions. In addition, water backdiffusion was observed using synchrotron X-ray radiography. These results support the explanation that backdiffusion plays a role in imparting drainability to the commercial-

sized PEFC and suggest that water drainage from both the cathode and anode is effective for water management.

In conclusion, we developed multi-scale water visualization techniques using operando neutron and synchrotron X-ray radiography to determine a strategy for three-dimensional water management, which is challenging in practical-sized PEFCs for FCEVs. The complementary use of neutron and synchrotron X-ray sources was used to evaluate the drainability of the second-generation MIRAI cell achieved through rational material design. These results show that backdiffusion is an important factor in determining the drainability of practical PEFCs.

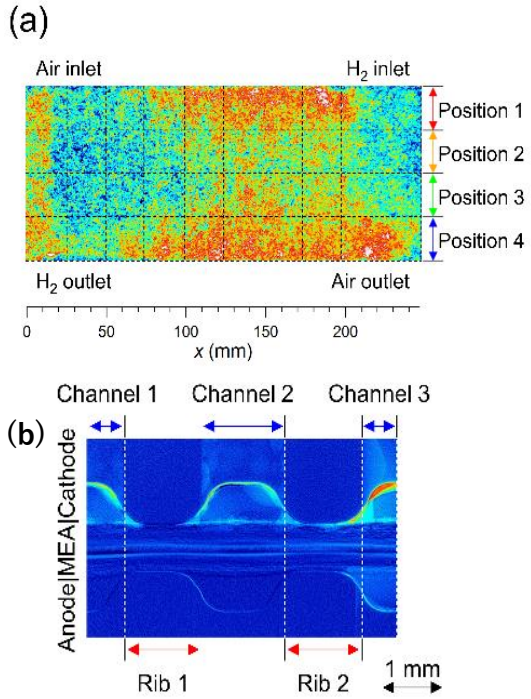

Fig. 3. Water distribution in PEFCs operating at a current density of 1.47 A cm^{-2} and a temperature of 60 ℃. (a) Water distribution in practical-sized cell visualized by neutron radiography. (b) Cross-sectional water distribution (120% RH) in hand-sized cell visualized by synchrotron radiation radiography. Reprinted with permission from [9]. Copyright 2023 American Chemical Society.

Yamaguchi Satoshi
Toyota Central R&D Labs., Inc.

References:

[1] Nonaka, T. et al. (2016). *AIP Conf. Proc.* **1741**, 030043.

[2] Nonaka, T. et al. (2012). *Rev. Sci. Instrum.* **83**, 083112.

[3] Makimura, Y. et al. (2016). *J. Electrochem. Soc.* **163**, A1450–A1456.

[4] Harada, M. et al. (2015). *SPring-8 User Experiment Report*, 2015A7003, 2015B7003.

[5] Setoyama, D. et al. (2015). *Proc. MECASENSE 2015*, 4.

[6] Hayashi, Y. et al. (2017). *SPring-8 User Experiment Report*, 2017A7002, 2017B7002.

[7] Hayashi, Y. et al. (2019). *Science* **366**, 1492–1496.

[8] Yamaguchi, S. et al. (2022). *J. Synchrotron Radiat.*, **29**, 1258–1264.

[9] Yoshimune, W. et al. (2023). *ACS Energy Lett.*, **8**, 3485–3487.